


## Article

# Structure Evolution of Ni<sub>36</sub>Al<sub>27</sub>Co<sub>37</sub> Alloy in the Process of Mechanical Alloying and Plasma Spheroidization

Alina K. Mazeeva <sup>1,\*</sup> , Artem Kim <sup>1</sup>, Nikolay E. Ozerskoi <sup>1</sup> , Aleksey I. Shamshurin <sup>1</sup> , Nikolay G. Razumov <sup>1</sup>, Denis V. Nazarov <sup>2</sup>  and Anatoliy A. Popovich <sup>1</sup>

<sup>1</sup> Institute of Machinery, Materials and Transport, Peter the Great St. Petersburg Polytechnic University, 29, Polytechnicheskaya Str., 195251 Saint Petersburg, Russia; artem\_7.kim@mail.ru (A.K.); nikolaiozerskoi@yandex.ru (N.E.O.); sham\_a@mail.ru (A.I.S.); n.razumov@inbox.ru (N.G.R.); popovicha@mail.ru (A.A.P.)

<sup>2</sup> Research Park “Innovative Technologies of Composite Nanomaterials”, St. Petersburg University, 13B Universitetskaya Emb., 199034 Saint Petersburg, Russia; dennazar1@yandex.ru

\* Correspondence: mazeevaalina@gmail.com

**Abstract:** In this paper, a novel approach to obtain a ferromagnetic material for smart applications was implied. A combination of mechanical alloying (MA) and plasma spheroidization (PS) was applied to produce Ni<sub>36</sub>Al<sub>27</sub>Co<sub>37</sub> spherical powder. Then its structure was systematically studied. It was shown that homogenization of the structure occurs due to mechanism of layered structure formation. The dependence of the lamella thickness on the energy dose input at MA was defined. It was found that 14.7 W·h/g is sufficient to obtain lamella thickness of 1 μm and less. The low-energy mode of a planetary mill with rotation speeds of the main disk/bowl of 150/–300 rpm makes it possible to achieve a uniform element distribution upon a minimal amount of impurity. During MA in an attritor Ni<sub>3</sub>Al-type intermetallic compounds are formed that result in more intensive degradation in particle size. Plasma spheroidization of the powder after MA allowed obtaining Ni<sub>36</sub>Al<sub>27</sub>Co<sub>37</sub> spherical powder. The powder had a fine β + γ-structure. The particle size distribution remains almost unchanged compared to the MA stage. Coercivity of the powder is 79 Oe. The powder obtained meets the requirements of selective laser melting technology, but also can be utilized as a functional filler in various magnetic composites.



**Citation:** Mazeeva, A.K.; Kim, A.; Ozerskoi, N.E.; Shamshurin, A.I.; Razumov, N.G.; Nazarov, D.V.; Popovich, A.A. Structure Evolution of Ni<sub>36</sub>Al<sub>27</sub>Co<sub>37</sub> Alloy in the Process of Mechanical Alloying and Plasma Spheroidization. *Metals* **2021**, *11*, 1557. <https://doi.org/10.3390/met11101557>

Academic Editors: Andrzej Miklaszewski and Francisco Paula Gómez Cuevas

**Keywords:** ferromagnetic smart alloy; plasma spheroidization; spherical powder; mechanical alloying; 4D-technology

Received: 3 August 2021

Accepted: 24 September 2021

Published: 29 September 2021

**Publisher's Note:** MDPI stays neutral with regard to jurisdictional claims in published maps and institutional affiliations.



**Copyright:** © 2021 by the authors. Licensee MDPI, Basel, Switzerland. This article is an open access article distributed under the terms and conditions of the Creative Commons Attribution (CC BY) license (<https://creativecommons.org/licenses/by/4.0/>).

## 1. Introduction

Ni-Al and Ni-Al-Co alloys are widely known and are traditionally used as heat-resistant alloys, in particular, in aviation. However, it is also known that they can exhibit the shape memory effect, which expands the possibilities of their use as structural materials and as functional ones.

Currently, the field of smart 4D materials manufacturing is actively developing [1]. It consists of the additive production of materials that change their characteristics under the influence of external factors. Among these materials, a special place is occupied by materials with a magnetically controlled shape memory effect (MCSME) [2], which makes it possible to obtain the deformation under the action of an external magnetic field. This deformation is several orders of magnitude higher than in traditional magnetostrictive materials. They can be used as sensors and as elements of smart structures and actuators of modern power drives. Actuators based on such materials make it possible to implement various types of movements, which will provide manufacturing of materials close to the capabilities of the human muscle. Using these materials allows to control vibration, adjust the size and shape of structural elements and prevent the formation and propagation of cracks in structures. There are also papers indicating the possibility of using MCSME alloy powders

as an internal sensor of mechanical stresses for timely prevention of critical destruction of the base metal when the powders are introduced into the base metal matrix [3,4].

The most studied alloys in this area are Ni-Mn-Ga Heusler alloys with a composition close to  $\text{Ni}_2\text{MnGa}$  [5], but their very high brittleness limits their applicability. The properties similar to those observed in the classical Heusler alloy are found in the structurally similar  $\text{Ni}_2\text{MnAl}$ ,  $\text{Co}_2\text{MnGa}$ ,  $\text{Co}_2\text{MnAl}$  alloys. The prospects of Ni-Al-Co alloys as alloys with MCSME were first shown by Japanese scientists [6].

In this system, shape memory effect (SME) is observed when the transformation B2 to  $\text{L}_{10}$  takes place [7]. In these alloys, B2 structure corresponds to the NiAl-type BCC-structure known as  $\beta$ -phase. The pure intermetallic compound is nonmagnetic and very brittle, though it also indicates SME. The addition of Co to Ni-Al alloys makes them ferromagnetic and more ductile due to the occurrence of  $\gamma$ -phase with FCC-structure [7,8]. The optimal composition to achieve appropriate functional and mechanical properties lies in a near-equiatomic ratio. Varying the elements contents in a narrow range also allows for varying martensitic transformation temperatures in a wide range [9]. For this work, the composition  $\text{Ni}_{36}\text{Al}_{27}\text{Co}_{37}$  is chosen according to papers [10–13], as it indicates SME at about room temperature, that can be used in a wide range of applications.

Conventional methods for its manufacturing include arc melting, vacuum melting, multi-pass rolling, and the following heat treatment. However, these technologies allow obtaining just typical items of standard shapes in large-scale production. In recent times, there is a new tendency to design unique metallic parts of complex geometries, where additive manufacturing (AM) technologies have become essential. The most technologically advanced methods to produce metallic parts are selective laser melting (SLM) and direct laser deposition (DLD) of the feedstock powder material or wire [14].

Since the main feedstock material for additive manufacturing of metallic parts is a powder [15,16], it will directly influence the quality of the finished product. Therefore, it meets specific requirements, such as appropriate chemical composition, a spherical shape, and a specific particle size of 15–120 microns for AM machines. However, in [17,18], the authors propose also to use irregular-shaped powders of MoSiBTiC composition obtained by high-energy ball milling for laser powder bed fusion as it is challenging to obtain spherical powders of this refractory composition with controllable particle size.

One of the universal methods to produce spherical powders of various compositions, including refractory ones [19–21] and with defined particle distribution, is plasma spheroidization [15,22–24]. The feedstock material for this process is a powder of any irregular shape. In order to obtain the initial powder of the required chemical composition, mechanical alloying can be effectively applied [22–24]. However, there are almost no published papers on the production of ferromagnetic Ni-Co-Al powders for 4D technologies.

This work aimed to investigate the structure and chemical composition of  $\text{Ni}_{36}\text{Al}_{27}\text{Co}_{37}$  powder in the process of its production by mechanical alloying of elemental powders and subsequent plasma spheroidization.

## 2. Materials and Methods

Elemental powders of Al (purity 99.5%) with a particle size of 100–150  $\mu\text{m}$ , Ni (purity 99.5%) with a particle size of 71–250  $\mu\text{m}$  and Co (purity 99.5%) with a particle size of 50–150  $\mu\text{m}$  were used as feedstock materials.

In order to obtain  $\text{Ni}_{36}\text{Al}_{27}\text{Co}_{37}$  powders, a combination of mechanical alloying (MA) and the following plasma spheroidization (PS) was used. At the MA stage, the elemental powders were mixed in a high-purity argon atmosphere according to the composition given. Then the mixture was milled with the addition of isopropyl alcohol in a vario-planetary mill (PIM) Fritsch Pulverisette 4 (Fritsch, Idar-oberstein, Germany) and in an attritor (A) Union Process SD-5 (Union Process, Akron, USA) in a high-purity argon atmosphere. For the vario-planetary mill, the following modes were applied: the ratio of the milled material mass to the milling balls mass was 1:20, rotation speeds of the main disc/bowl were 150/–300, 200/–400, 200/–600 rpm. For the attritor, the following mode was applied: the

ratio of the milled material mass to the milling balls mass was 1:20, the rotation speed of the turner was 250 rpm. MA duration was 5–20 h with a step of 5 h. Every 15 min, there was a pause of 15 min to prevent an overheating of the milling system.

The spheroidization was carried out by induction plasma treatment in the Tek-15 device (Tekna Plasma Systems Inc., Sherbrooke, Canada). An argon-hydrogen mixture was used as a plasma-forming gas. The following mode was applied: plasmatron power—15 kW, pressure—15 psi, powder feed rate—27 g/min, Ar flow rate—40 L/min, H<sub>2</sub> flow rate—4 L/min, injection point—0 (in the center of the induction coil).

Powders morphology, structure, chemical composition, and element distribution over cross-sections were investigated using a scanning electron microscope Tescan Mira 3 LMU (Tescan Orsay Holding, Brno, Czech Republic) equipped with a specialized attachment for energy dispersive X-ray spectral analysis. Polished sections of the powders were used to analyze the structure, chemical composition, and element distribution. Etched sections were investigated by using an optical microscope Leica DMi8 (Leica Microsystems, Wezlar, Germany). The etching was carried out by using Marble's reagent.

Sample phase compositions were investigated by using the X-ray diffractometer (XRD) Bruker D8 Advance (Bruker Corporation, Billerica, USA) with Cu-K $\alpha$ -radiation. The data analysis was carried out by using Evaluation software and the diffraction database PDF-2.

Calculations of expected phase compositions were performed by the CALPHAD method using Thermo-Calc 2020a software equipped with TCHEA4 database (Thermo-Calc Software AB, Solna, Sweden).

Powder particle size distribution was investigated by using the laser diffractometer Analysette 22 NanoTec plus setup (Fritsch, Idar-oberstein, Germany). When analyzing the data, D10, D50, and D90 mean that 10%, 50%, and 90% of particles, respectively, have a size less than the corresponding value. For example, D50 = 15  $\mu$ m means that the size of 50% of the particles is less than 15  $\mu$ m.

Magnetic properties were measured by using a vibrating sample magnetometer Lake Shore 7410 (Lake Shore Cryotronics, Inc., Westerville, USA).

### 3. Results

#### 3.1. Mechanical Alloying

In the process of powder production, the stage of mechanical alloying is used to obtain a powder of a given composition from the initial powders avoiding the melting stage.

The main goal and criterion of MA completeness is a uniform chemical composition of the whole powder and its individual particles.

In order to compare various modes of MA at different mills, the parameters of process power  $W$  and input energy  $E$  are used. These parameters for a planetary mill can be calculated according to theory [25] by using the following equations:

$$E = W \cdot t \quad (1)$$

where  $t$ —MA duration time

$$W = (2 * \pi)^2 * M * v_p^3 * R_p * (D_v - D_b) * (1 - \chi) * (2 - \frac{v_v}{v_p})W \quad (2)$$

where  $M$  is a mass of the milling balls,  $v_p$  is the rotation speed of the main disk of the mill,  $R_p$  is the disk radius,  $D_v$  is the mill bowl diameter,  $D_b$  is the milling ball diameter,  $\chi$  is the filling ratio of the milling balls,  $v_v$  is the rotation speed of the bowl including its sign.

According to Equation (2), the dependences of MA power on the rotation speeds of the main disk and the bowl of Fritsch Pulverisette 4 mill were plotted (Figure 1).

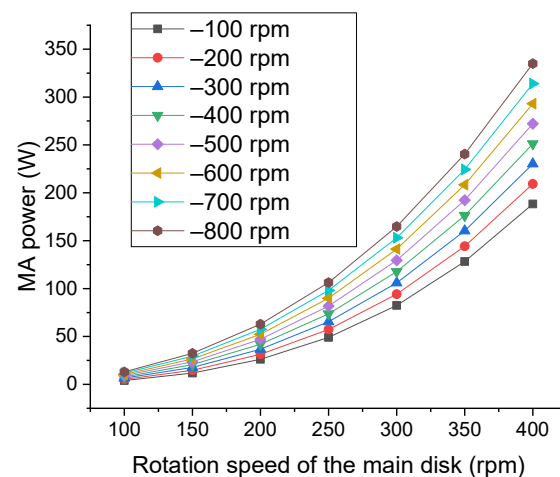


**Figure 1.** Calculated dependences of MA power on rotation speeds of the main disk and the bowls of Fritsch Pulverisette 4 mill.

Figure 1 allows choosing the rotation speed of the working parts of the mill to obtain MA power required and to calculate the energy dose  $D$  according to the following equation:

$$D = E/m \quad (3)$$

where  $m$  is the mass of the milled material.

For the modes studied, the energy parameters are calculated and presented in Table 1.

**Table 1.** Energy parameters of MA modes in the planetary mill and their influence on Fe-impurity quantity.

Mode	W, W	t, h	D, W·h/g	Fe, wt.%
150/−300	18	5	2.9	0.07
		10	5.9	0.13
		15	8.8	0.17
		20	11.8	0.18
		25	14.7	0.31
200/−400	42	5	7.0	0.40
		10	14.0	1.07
		15	20.9	1.27
		20	27.9	1.74
200/−600	52	5	8.7	0.60
		10	17.4	2.46
		15	26.2	3.14
		20	34.9	2.99

Figure 2 shows the structure of the MA powder after different milling modes. It can be seen that a layered composite with visible lamellae is first formed.

With an increase in MA energy dose, the thickness of the lamellae decreases (Figure 2). It can be seen that after five hours of MA at the lowest-energy mode 150/−300, when the energy dose is 2.9 W·h/g some thick lamellae are not sufficiently flattened (Figure 2a). However, the thickness does not exceed 10–12  $\mu\text{m}$ . Moreover, after 25 h of MA at this mode, when the energy dose is 14.7 W·h/g, the maximal thickness observed is about 1.1  $\mu\text{m}$ .



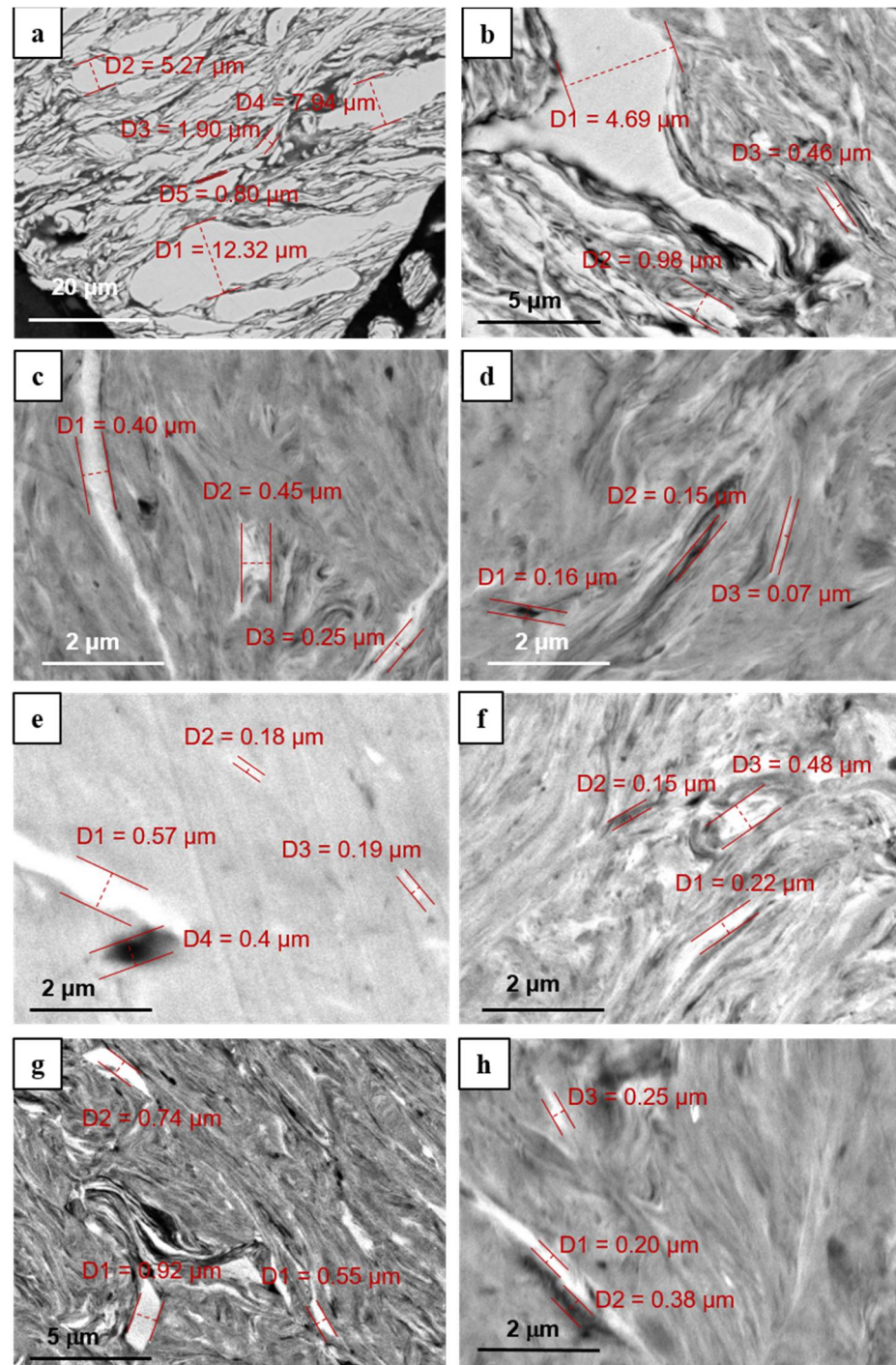


**Figure 2.** BSE-images of  $\text{Ni}_{36}\text{Al}_{27}\text{Co}_{37}$  powders after MA in the planetary mill (a–f) and in the attritor (g,h) at the modes (a) 150/−300 5 h; (b) 150/−300 15 h; (c) 150/−300 25 h; (d) 200/−400 15 h; (e) 200/−600 15 h; (f) 200/−400 20 h; (g) 250 4.5 h; and (h) 250 10 h.

Element distribution at the modes with energy doses of 14.7 W·h/g and higher is presented in Figure 3. It can be seen that the minimum time required for complete mixing of the elements in  $\text{Ni}_{36}\text{Al}_{27}\text{Co}_{37}$  composition is 15 h at 200/−600 mode, 20 h—at 200/−400 mode, and 25 h at 200/−600 mode.

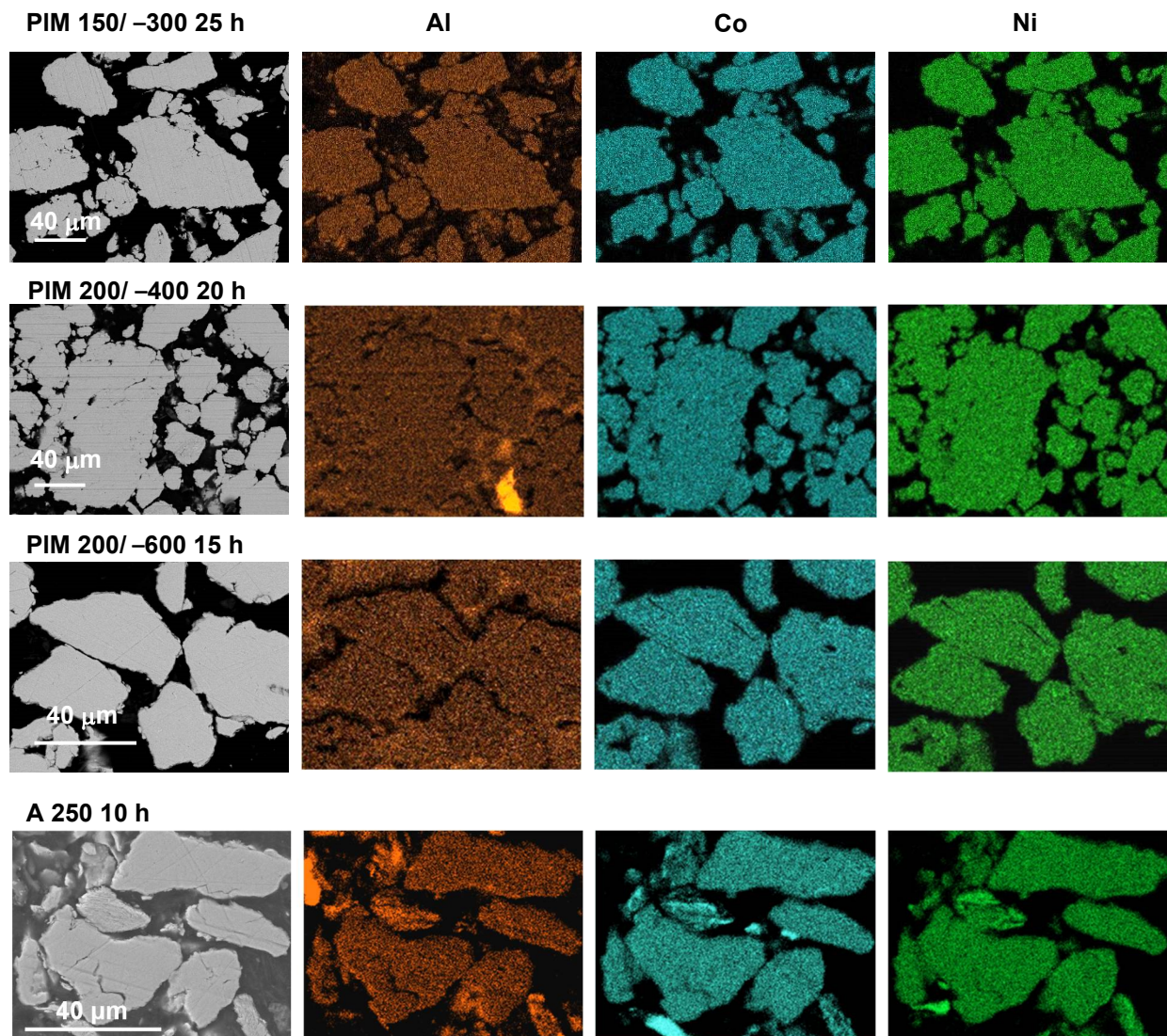


**Figure 3.** Element distribution in  $\text{Ni}_{36}\text{Al}_{27}\text{Co}_{37}$  MA-powders at various MA modes and time of milling in the planetary mill (PIM) and in the attritor (A).

Figure 4a shows XRD patterns of the milled powder after different times of MA at mode 200/–400. The diffraction peaks from the initial elements gradually broaden, and their intensity decreases, while the peaks of aluminum are the first to disappear, which indicates that aluminum dissolves first in the composition studied. Then hexagonal cobalt dissolves, passing into a solid solution (Co, Ni) with an FCC lattice.

In the present work, another technique of MA was also studied. The technique included milling in an attritor. This technique has the advantage of higher productivity than milling in the planetary mill and can be used to produce a sufficient amount of the powder for further use in additive manufacturing. In the attritor, the working container where the MA process is performed is fixed and is not rotated. XRD analysis shows that when the initial powders are milled in the attritor, not only a dissolution of initial elements takes place, but also an intermetallic compound of  $\text{Ni}_3\text{Al}$ -type with Pm3m lattice is formed (Figure 4b).



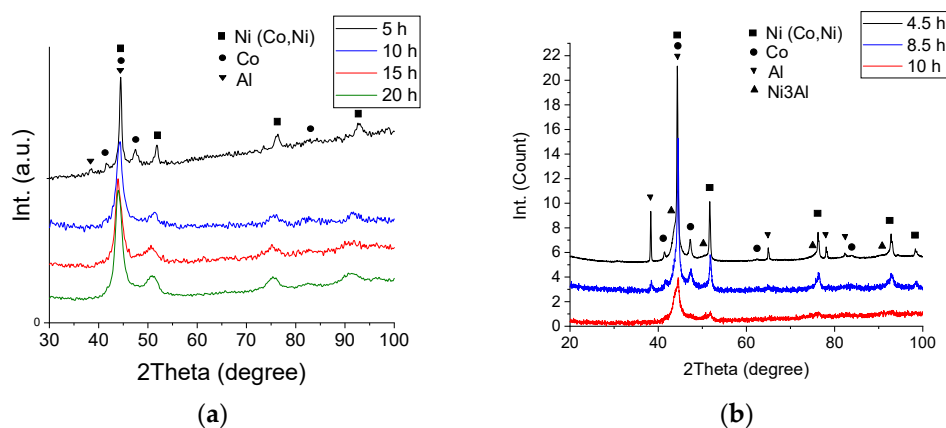


**Figure 4.** XRD-patterns of  $\text{Ni}_{36}\text{Al}_{27}\text{Co}_{37}$  powders produced by mechanical alloying in planetary mill at 200/−400 mode (a), and in attritor (b).

After ten hours of mechanical alloying in the attritor, the  $\text{Ni}_{36}\text{Al}_{27}\text{Co}_{37}$  powder with the particle size distribution  $D_{10} = 4 \mu\text{m}$ ;  $D_{50} = 15 \mu\text{m}$ ;  $D_{90} = 32 \mu\text{m}$  was achieved. The average size of the particles after MA in attritor is noticeably lower than the size after MA in the planetary mill. After ten hours of MA in the planetary mill at the highest energy mode 200/−600, the particle size distribution was  $D_{10} = 18 \mu\text{m}$ ;  $D_{50} = 42 \mu\text{m}$ ;  $D_{90} = 84 \mu\text{m}$ . This difference can be explained by some differences in MA mechanisms implied in these types of mills and is discussed in detail in the Discussion Section.

### 3.2. Plasma Spheroidization

After mechanical alloying, the powder was treated in a low-temperature plasma jet to put the particles into a spherical shape. Figure 5 shows the morphology of  $\text{Ni}_{36}\text{Al}_{27}\text{Co}_{37}$  powder particles after PS. As shown in the figure, the irregular-shaped particles formed at the MA stage become spherical after PS. However, it can also be noted that many submicron particles are present on the surface of the spherical particles, which is explained by the presence of small particles in the initial powder. The presence of the submicron particles leads to a deterioration in the fluidity of the powder and malfunctions of additive machines. In order to remove submicron particles, the PS-powder was subjected to air classification and then was treated in an ultrasonic bath with isopropyl alcohol.

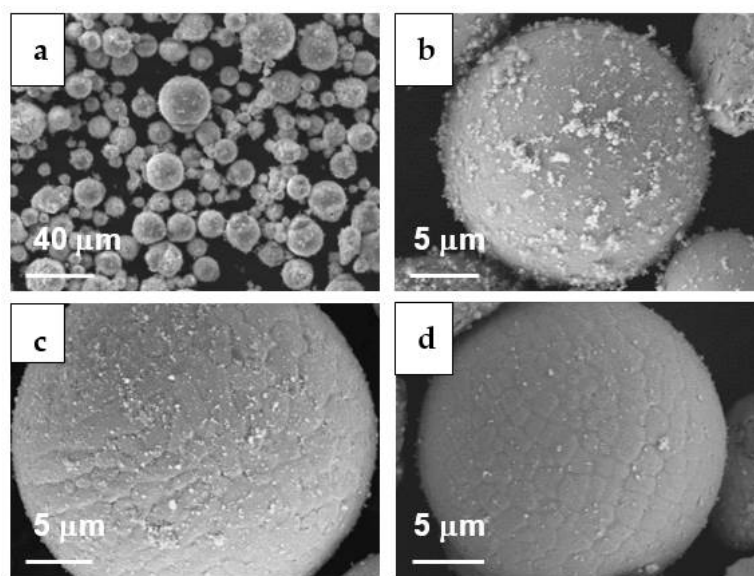


**Figure 5.** SEM-images of  $\text{Ni}_{36}\text{Al}_{27}\text{Co}_{37}$  powder after plasma spheroidization: (a) magnification 1000; (b) magnification 10,000 (c) after PS and air classification and (d) after PS, air classification and ultrasonic treatment.

As a result of the air classification, the number of the submicron particles is significantly reduced (Figure 5c), ultrasonic treatment allows removal of some of the remaining submicron particles (Figure 5d). After the ultrasonic treatment, a certain amount of submicron particles remains, associated with the overall small size of the spherical particles, complicating the powder's cleaning. However, according to the particle size distribution analysis, the total content of particles with a size less than 1  $\mu\text{m}$  does not exceed 1%. The general particle size distribution after all three treatments was as follows  $D_{10} = 12 \mu\text{m}$ ,  $D_{50} = 22 \mu\text{m}$ ,  $D_{90} = 37 \mu\text{m}$ , which is higher than for the powder after MA in the attritor due to removal of submicron particles at the stages of air classification and treatment in the ultrasonic bath. However, the difference in the maximal size of the particles is insignificant. Therefore, it can be considered that the general particle size of the powders obtained by MA almost does not change after PS.

Figure 5c,d also shows that the spherical particles of  $\text{Ni}_{36}\text{Al}_{27}\text{Co}_{37}$  powder have a cast surface structure with a grain size of about 1  $\mu\text{m}$  that is clearly visible. Such a structure is typical for powders obtained by plasma spheroidization [22–24].

Plasma spheroidization leads to a change in the chemical composition of the alloy. It can be seen in Table 2 that aluminum content is reduced by about 1 wt.%. This phenomenon can be explained by the fact that aluminum has significantly lower melting and boiling points (660 and 2470  $^{\circ}\text{C}$ , respectively) than nickel (1453 and 2732  $^{\circ}\text{C}$ , respectively) and cobalt (1495 and 2870  $^{\circ}\text{C}$ , respectively), that leads to more intensive evaporation of aluminum even when the powder remains in the low-temperature plasma jet for a short time.

**Table 2.** Chemical compositions of  $\text{Ni}_{36}\text{Al}_{27}\text{Co}_{37}$  powder after mechanical alloying and subsequent plasma spheroidization.

Production Stage	Al		Fe		Ni		Co	
	wt.%	at.%	wt.%	at.%	wt.%	at.%	wt.%	at.%
MA	14.20	26.53	0.31	0.28	42.17	36.22	43.32	37.07
PS	13.27	25.01	0.37	0.34	42.74	37.02	43.62	37.64

Analysis of the phase composition of the powder after PS showed that the powder contains  $\gamma$ -phase with Fm-3m (225) crystal lattice and  $\beta$ -phase with Im-3m (229) crystal lattice (Figure 6). In the optical micrograph of an etched powder section,  $\gamma$ -phase is represented by light areas, and  $\beta$ -phase is represented by the dark ones [8,26]. It is also confirmed by element distribution maps (Figure 7), where regions enriched with Co correspond to  $\gamma$ -phase and regions enriched with Al correspond to  $\beta$ -phase [7,27]. The latter possesses a B2 structure, and there are no diffraction peaks from the  $L1_0$  structure; thus, the temperature of the direct martensitic transformation start is below room temperature in the resulting powder.

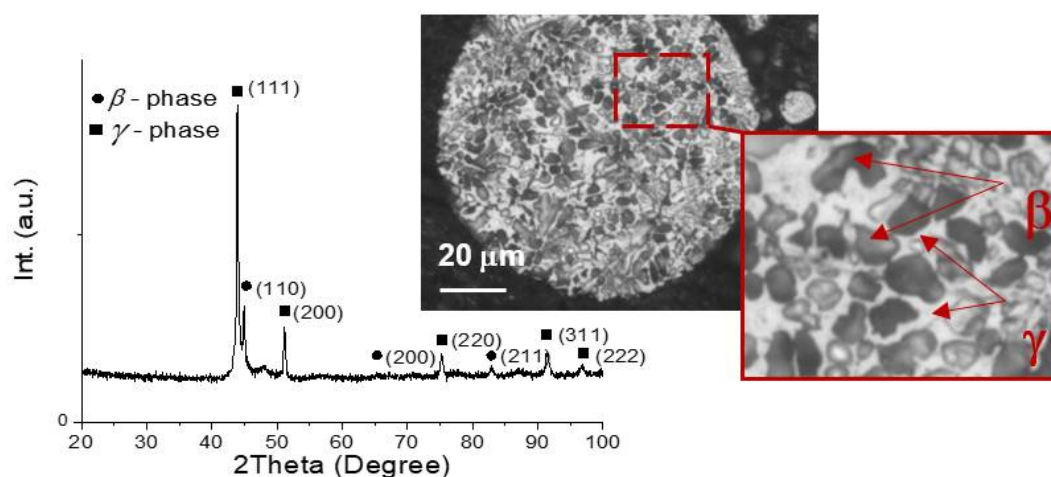


**Figure 6.** X-ray diffraction pattern and micrograph of  $\text{Ni}_{36}\text{Al}_{27}\text{Co}_{37}$  powder after plasma spheroidization.



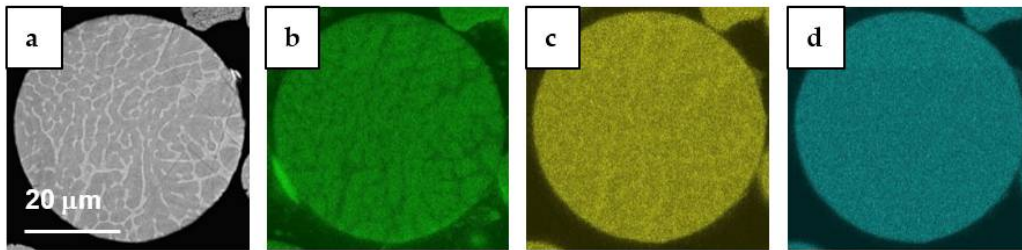


**Figure 7.** Element distribution in  $\text{Ni}_{36}\text{Al}_{27}\text{Co}_{37}$  powder particle after spheroidization: (a) BSE-image of the area investigated, (b) Al, (c) Co and (d) Ni.

According to quantity estimation, the phase ratio in the spherical powder after treatment in the plasma jet was as follows:  $\beta$ -phase—21% and  $\gamma$ -phase—79%, the average grain size of the  $\beta$ -phase was about 5  $\mu\text{m}$ .

Figure 8 shows the magnetic hysteresis loop for the spherical powder after PS. The coercive force is determined from the magnetic hysteresis loop. Its value is 79 Oe.

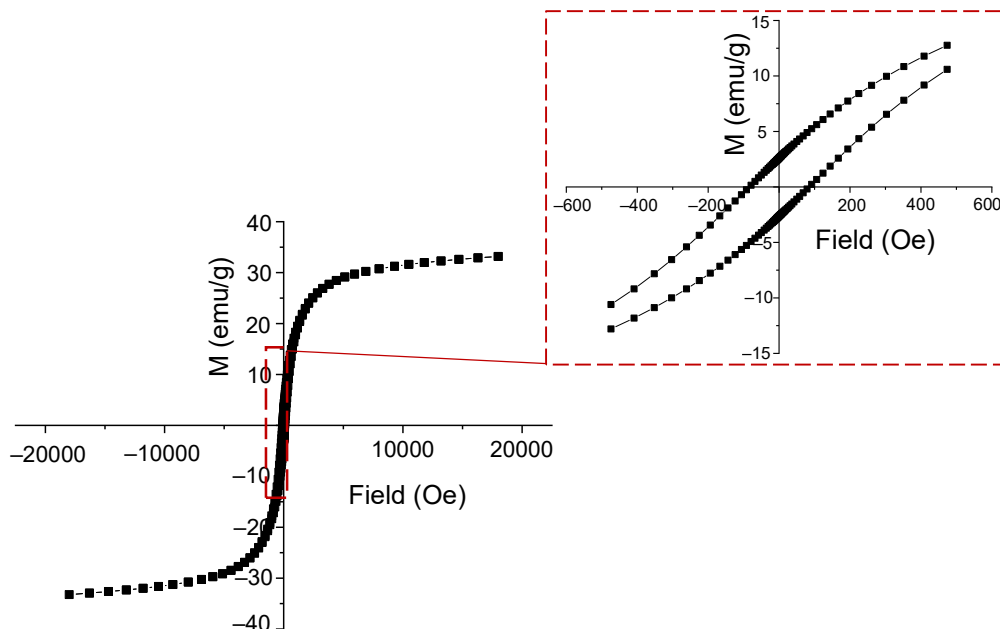


**Figure 8.** Magnetic hysteresis loop of  $\text{Ni}_{36}\text{Al}_{27}\text{Co}_{37}$  powder after PS.

## 4. Discussion

### 4.1. Mechanical Alloying

Investigation into the structure formation process in MA powders showed that a layered composite with visible lamellae is first formed. This type of structure is formed because all elements in the composition studied are ductile, and under the intense mechanical action, the particles of the elemental powders begin to coat each other. According to the data calculated and the SEM study, the dependence of the lamella thickness on the MA energy dose was plotted (Figure 9). For each mode, at least 30 values of lamella thickness were used. It can be seen that even a comparatively low energy dose of about 3  $\text{W}\cdot\text{h/g}$  leads to the formation of lamellae with a thickness of less than 10–12  $\mu\text{m}$  in  $\text{Ni}_{36}\text{Al}_{27}\text{Co}_{37}$  composition. However, a higher energy dose leads to a higher uniformity of lamella thickness distribution. It can also be noted that at the energy dose of 14.7  $\text{W}\cdot\text{h/g}$  and higher, the thickness of the lamellae almost does not change, and the thickness does not exceed 1  $\mu\text{m}$ , though the uniformity of the lamella thickness distribution slightly increases.

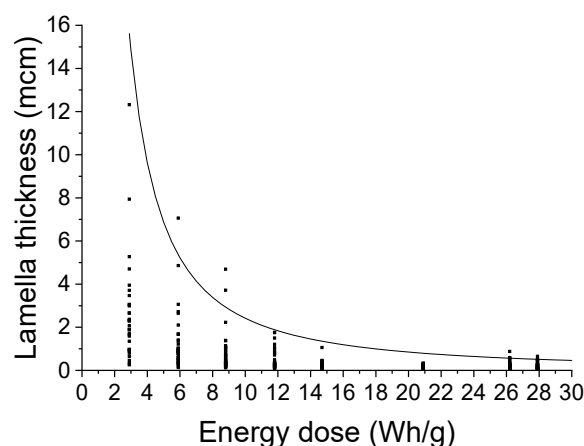


**Figure 9.** Dependence of lamella thickness in  $\text{Ni}_{36}\text{Al}_{27}\text{Co}_{37}$  powder on MA energy dose.

It can be interpreted that the minimal lamella thickness achieved by MA for  $\text{Ni}_{36}\text{Al}_{27}\text{Co}_{37}$  alloy is about 1  $\mu\text{m}$ . Further increase in energy dose does not lead to a sufficient decrease in lamella thickness, though durable mechanical alloying can result in nanostructured [28] and amorphous state [29] due to solid-phase diffusion caused by the intensive mechanical impact of the process of MA. However, for subsequent plasma spheroidization, the lamella thickness of 1  $\mu\text{m}$  after MA can be considered fine enough, and the powder can be taken as an alloy with homogeneous composition and structure. Such elemental powders, deeply diffused in each other, prevent segregation formation during subsequent plasma spheroidization [22,23,30]. The sufficient homogeneity is also confirmed by element distribution analysis (Figure 3).

Since the energy dose is adjusted by the MA mode and the MA duration, high-energy modes decrease the required time of MA. However, using such modes also leads to a more intensive mechanical impact on the milling balls. It results in impurities in the milled material. In this work, steel milling balls were used; hence the main impurity in the powders studied is Fe. There is no direct relationship between the energy dose and the Fe amount in the MA-powder, though using higher-energy modes with higher rotation speeds leads to higher impurity contamination. For example, after 25 h of MA at 150/−300 mode, Fe content is about 0.3 wt.%, while after 10 h of MA at 200/−600 mode, it is about 2.5 wt.% (Table 1). Thus, low-energy modes are more preferable to use.

The changes in the structure of the powders after different MA modes were investigated by XRD analysis are similar. It differs in dissolution rates. After 20 h of MA at the lowest-energy mode 150/−300, weak peaks of elemental cobalt are still present. Higher-energy modes 200/−400 and 200/−600 lead to complete dissolution of the components in each other, already after 5–10 h. At the same time, at the highest-energy mode 200/−600, an increase in MA duration time results in a shift of the diffraction peaks towards smaller angles that can be associated with an induction of significant distortions as a result of intense mechanical impact on the material and with an increase in the lattice parameter of the solid solution (Co, Ni) due to the continuing process of dissolution of the initial components in it.

When discussing the MA process in the attritor, it should be taken into account that the energy intensity in this case was calculated according to the model described in [25] and is 2760 W, which is relatively high. Despite the rather low specific energy intensity of 1.38 W/g in this case, that is due to a significantly higher powder volume; there can occur some local effects, particularly a significant increase in local temperatures. Hence high local temperatures may result in  $\text{Ni}_3\text{Al}$ -type intermetallic compound formation even when having a short effect.

When milling ductile components, the action of two competing processes is observed. The first one is an enlargement of the particles due to a mechanism similar to cold welding [31], and the second one is a reduction of the particle size due to the destruction of the

particles under intense mechanical impact. Along with a higher total energy intensity in the attritor than the planetary mill, the presence of the brittle intermetallic compound leads to more intense destruction of the material and a particle size reduction. In addition, when alloying in an attritor, the powder milling occurs mainly due to rubbing without shock effects, as opposed to the planetary mill. Furthermore, this mechanism is more effective in grinding ductile materials. Thus, after 10 h of MA in the attritor, the particle size distribution of  $\text{Ni}_{36}\text{Al}_{27}\text{Co}_{37}$  powder was as follows:  $D_{10} = 4 \mu\text{m}$ ;  $D_{50} = 15 \mu\text{m}$ ;  $D_{90} = 32 \mu\text{m}$ , while after 10 h of MA in the planetary mill at the highest energy mode 200/–600, the particle size distribution was  $D_{10} = 18 \mu\text{m}$ ;  $D_{50} = 42 \mu\text{m}$ ;  $D_{90} = 84 \mu\text{m}$ . The action of attrition can also explain it in the attritor that leads to more intensive particle size degradation than at impact action in the planetary mill in the case of ductile components.

#### 4.2. Plasma Spheroidization

Plasma spheroidization allowed the transformation of the irregular-shaped MA powder to a spherical-shaped one. The initial MA-powder was rather fine with the average particle size of  $15 \mu\text{m}$ , which led to a large number of submicron particles in the powder. The small particles melt and evaporate much faster than the bulk of larger particles and then condense on the formed spherical particles [24,32]. This observation makes it necessary to imply subsequent classification and ultrasonic treatment to eliminate the submicron particles and increase the spherical powder's technological characteristics. These steps lead to an increase in the number of bigger particles indicated by the values of  $D_{10} = 12 \mu\text{m}$  and  $D_{50} = 22 \mu\text{m}$ . However, the general size of the particles indicated by  $D_{90}$  is almost the same. Therefore, it can be considered that the particle size distribution of the powders obtained by MA almost does not change after PS.

XRD analysis of the PS-powder showed that the  $\beta$ - $\gamma$  phases ratio significantly differs from the expected one. It was expected that the phase composition of the powder after PS should have corresponded to a high-temperature state due to the rapid solidification of the melted particles in the PS process. According to the calculations by using the CALPHAD method, the content of  $\gamma$ -phase decreases with an increase in temperature. However, even at  $900 \text{ }^\circ\text{C}$ ,  $\text{Ni}_{36}\text{Al}_{27}\text{Co}_{37}$  alloy should contain 26% of  $\gamma$ -phase. Considering that after PS, the actual composition is close to  $\text{Ni}_{37}\text{Al}_{25}\text{Co}_{38}$ , the alloy should contain 36% of  $\gamma$ -phase at the temperature of  $950 \text{ }^\circ\text{C}$ . However, at the temperatures below this value,  $\text{Ni}_{37}\text{Al}_{25}\text{Co}_{38}$  alloy contains two FCC-phases, the composition of the second FCC-phase is intermediate between  $\beta$ - and  $\gamma$ -phases. The total amount of FCC-phases is about 50% in this case. The difference is experimentally estimated, and the expected content of  $\gamma$ -phase can be explained both by the presence of the second FCC-phase and impurities of Fe and others.

As a result of the PS of the powder obtained by MA in the attritor, a spherical-shaped  $\text{Ni}_{36}\text{Al}_{27}\text{Co}_{37}$  powder with particle sizes in the range from  $D_{10} = 12 \mu\text{m}$  to  $D_{90} = 37 \mu\text{m}$  was obtained. Therefore, the particle size distribution and the particle shape are acceptable for using the powder in selective laser melting machines.

Since the  $\text{Ni}_{36}\text{Al}_{27}\text{Co}_{37}$  powder is planned to use as a feedstock material for ferromagnetic smart applications, it is essential to evaluate its magnetic properties. Coercivity depends heavily on the structural state of a material, and as a consequence, a method of its manufacture and the following treatment is capable of changing this property in a quite significant way. The alloys of close to  $\text{Ni}_{36}\text{Al}_{27}\text{Co}_{37}$  compositions obtained by conventional methods of arc melting and subsequent heat treatment show the coercivity from 0.7 to 60 Oe [33–35]. Thin ribbons of the alloys obtained by rapid quenching show the coercivity from 100 to 2000 Oe [36], and the alloys obtained by conventional methods of powder metallurgy such as sintering the powders show the coercivity of about 160 to 190 Oe [37]. Thus, the spherical  $\text{Ni}_{36}\text{Al}_{27}\text{Co}_{37}$  powder obtained in the present work is between the alloys produced by arc melting and the alloys produced by conventional methods of PM by its magnetic properties and can be used not only as a feedstock material for selective laser melting but also as a functional filler in various magnetic composites.



## 5. Conclusions

In this work, a spherical-shaped  $\text{Ni}_{36}\text{Al}_{27}\text{Co}_{37}$  powder was obtained. In addition, the evolution of its structure after various technological operations was investigated.

- (1) It was demonstrated that in the process of milling of the initial powders of Al, Co, and Ni in the planetary mill, the formation of the alloy occurs according to the mechanism of interaction of plastic components with the formation of a layered structure. With an increase in the MA energy dose adjusted by MA modes and duration time, the lamella thickness in the layered structure decreases from the maximal values of about  $12\ \mu\text{m}$  (after 5 h of MA at 150/−300 mode) to about  $1\ \mu\text{m}$ . It is shown that the minimal energy dose to achieve an appropriate homogenized structure is  $14.7\ \text{W}\cdot\text{h}/\text{g}$ .
- (2) It was shown that the lowest-energy mode with rotation speeds of the main disc and the bowl of −150 and 300 rpm, respectively, can significantly reduce the amount of Fe impurity. A homogeneous element distribution over the volume of particles was achieved after 25 h of MA at this mode; the amount of Fe impurity does not exceed the acceptable 0.5 wt.%.
- (3) It was found that the milling of the initial powders in an attritor leads to the formation of  $\text{Ni}_3\text{Al}$ -type intermetallic compound, which, along with the high total energy intensity of the process, leads to a more intense particle size reduction than after MA in the planetary mill. The particle size distribution after 10 h of MA in the attritor is from  $D_{10} = 4\ \mu\text{m}$  to  $D_{90} = 32\ \mu\text{m}$ , while after 10 h of MA in the planetary mill at the highest-energy mode 200/−600, the particle size distribution is  $D_{10} = 18\ \mu\text{m}$ ;  $D_{50} = 42\ \mu\text{m}$ ;  $D_{90} = 84\ \mu\text{m}$ .
- (4) As a result of the subsequent plasma spheroidization, the irregular-shaped particles of the MA-powder were spheroidized. The spherical particles have the morphology of a cast surface. The particle size of the powders obtained by MA indicated by  $D_{90}$  almost does not change after PS. However,  $D_{10}$  and  $D_{50}$  change significantly due to the elimination of small particles by subsequent air classification and ultrasonic treatment. The structure of the powder particles consists of  $\beta$ - and  $\gamma$ -phases with a grain size of about  $5\ \mu\text{m}$ . The phase ratio is as follows: 21% of  $\beta$ -phase and 79% of  $\gamma$ -phase significantly differ from the calculated values. This phenomenon can be explained by the presence of the second FCC phase and impurities of Fe and others.
- (5) It was found that after PS, the content of the most low-melting element Al is reduced by 1 wt.% compared to the powder after MA, which must be considered when calculating the initial ratio of components to obtain a given composition.
- (6) The particle size distribution from  $D_{10} = 12\ \mu\text{m}$  to  $D_{90} = 37\ \mu\text{m}$  and the spherical shape of the particles obtained are acceptable for using the powder in selective laser melting machines.
- (7) Coercivity of the spherical  $\text{Ni}_{36}\text{Al}_{27}\text{Co}_{37}$  powder obtained is 79 Oe. This allows the use of the powder not only as a feedstock material for selective laser melting, it can also be used as a functional filler in various magnetic composites.

**Author Contributions:** Conceptualization, A.K.M. and N.G.R., methodology, N.G.R., formal analysis, A.K. and N.G.R., investigation, A.K.M., A.K., A.I.S., N.E.O. and D.V.N., writing—original draft preparation, A.K.M., writing—review and editing, A.K. and N.G.R., supervision, A.A.P., project administration, A.K.M., funding acquisition, A.K.M. All authors have read and agreed to the published version of the manuscript.

**Funding:** This research was funded by the Russian Science Foundation grant (project № 20-79-00061).

**Institutional Review Board Statement:** Not applicable.

**Informed Consent Statement:** Not applicable.

**Data Availability Statement:** Data is contained within the article.

**Acknowledgments:** Magnetic properties were measured using the equipment of the resource center of the Research Park St. Petersburg State University, “Innovative Technologies of Composite Nanomaterials”.

**Conflicts of Interest:** The authors declare no conflict of interest.

## References

1. Joshi, S.; Rawat, K.; Karunakaran, C.; Rajamohan, V.; Mathew, A.T.; Koziol, K.; Kumar Thakur, V.; Balan, A.S.S. 4D printing of materials for the future: Opportunities and challenges. *Appl. Mater. Today* **2020**, *18*, 100490. [[CrossRef](#)]
2. Faran, E.; Shilo, D. Ferromagnetic Shape Memory Alloys—Challenges, Applications, and Experimental Characterization. *Exp. Tech.* **2016**, *40*, 1005–1031. [[CrossRef](#)]
3. Yamakov, V.; Hochhalter, J.D.; Leser, W.P.; Warner, J.E.; Newman, J.A.; Purja Pun, G.P.; Mishin, Y. Multiscale modeling of sensory properties of Co–Ni–Al shape memory particles embedded in an Al metal matrix. *J. Mater. Sci.* **2016**, *51*, 1204–1216. [[CrossRef](#)]
4. Barta, N.E.; Karaman, I. Embedded magnetic shape memory particles in lightweight composites for crack detection. *Mater. Sci. Eng. A* **2019**, *751*, 201–213. [[CrossRef](#)]
5. Yu, G.H.; Xu, Y.L.; Liu, Z.H.; Qiu, H.M.; Zhu, Z.Y.; Huang, X.P.; Pan, L.Q. Recent progress in Heusler-type magnetic shape memory alloys. *Rare Met.* **2015**, *34*, 527–539. [[CrossRef](#)]
6. Oikawa, K.; Wulff, L.; Iijima, T.; Gejima, F.; Ohmori, T.; Fujita, A.; Fukamichi, K.; Kainuma, R.; Ishida, K. Promising ferromagnetic Ni–Co–Al shape memory alloy system. *Appl. Phys. Lett.* **2001**, *79*, 3290–3292. [[CrossRef](#)]
7. Zhou, F.; Zhou, Y.; Wang, J.; Liang, J.; Gao, H.; Kang, M. Enlightening from  $\gamma$ ,  $\gamma'$  and  $\beta$  phase transformations in Al–Co–Ni alloy system: A review. *Curr. Opin. Solid State Mater. Sci.* **2019**, *23*, 100784. [[CrossRef](#)]
8. Tanaka, Y.; Ohmori, T.; Oikawa, K.; Kainuma, R.; Ishida, K. Ferromagnetic Co–Ni–Al Shape Memory Alloys with  $\beta + \gamma$  Two-Phase Structure. *Mater. Trans.* **2004**, *45*, 427–430. [[CrossRef](#)]
9. Tanaka, Y.; Oikawa, K.; Sutou, Y.; Omori, T.; Kainuma, R.; Ishida, K. Martensitic transition and superelasticity of Co–Ni–Al ferromagnetic shape memory alloys with  $\beta + \gamma$  two-phase structure. *Mater. Sci. Eng. A* **2006**, *438–440*, 1054–1060. [[CrossRef](#)]
10. Kositsyna, I.I.; Zavalishin, V.A. Study of Co–Ni–Al alloys with magnetically controlled shape memory effect. *Mater. Sci. Forum* **2010**, *635*, 75–80. [[CrossRef](#)]
11. Valiullin, A.I.; Kositsyna, I.I.; Kositsyn, S.V.; Kataeva, N.V. Stabilization of high-temperature shape memory effect in functional Ni–Al–Co martensitic alloys. *Mater. Sci. Eng. A* **2008**, *481–482*, 551–554. [[CrossRef](#)]
12. Valiullin, A.I.; Kositsyn, S.V.; Kositsina, I.I.; Kataeva, N.V.; Zavalishin, V.A. Study of ferromagnetic Co–Ni–Al alloys with thermoelastic L10 martensite. *Mater. Sci. Eng. A* **2006**, *438–440*, 1041–1044. [[CrossRef](#)]
13. Ju, J.; Xue, F.; Sun, L. Structure and Performance Changes of Ni–Co–Al Shape Memory Alloys in Relation to Co/Al Atomic Ratio. *J. Iron Steel Res. Int.* **2015**, *22*, 652–656. [[CrossRef](#)]
14. DebRoy, T.; Wei, H.L.; Zuback, J.S.; Mukherjee, T.; Elmer, J.W.; Milewski, J.O.; Beese, A.M.; Wilson-Heid, A.; De, A.; Zhang, W. Additive manufacturing of metallic components—Process, structure and properties. *Prog. Mater. Sci.* **2018**, *92*, 112–224. [[CrossRef](#)]
15. Dawes, J.; Bowerman, R.; Trepleton, R. Introduction to the additive manufacturing powder metallurgy supply chain. *Johnson Matthey Technol. Rev.* **2015**, *59*, 243–256. [[CrossRef](#)]
16. Saheb, S.H.; Durgam, V.K.; Chandrashekar, A. A review on metal powders in additive manufacturing. *AIP Conf. Proc.* **2020**, *2281*, 020018. [[CrossRef](#)]
17. Zhou, Z.; Guo, S.; Zhou, W.; Nomura, N. A novel approach of fabricating monodispersed spherical MoSiBTiC particles for additive manufacturing. *Sci. Rep.* **2021**, *11*, 16576. [[CrossRef](#)] [[PubMed](#)]
18. Zhou, W.; Sun, X.; Tsunoda, K.; Kikuchi, K.; Nomura, N.; Yoshimi, K.; Kawasaki, A. Powder fabrication and laser additive manufacturing of MoSiBTiC alloy. *Intermetallics* **2019**, *104*, 33–42. [[CrossRef](#)]
19. Goncharov, I.S.; Razumov, N.G.; Silin, A.O.; Ozerskoi, N.E.; Shamshurin, A.I.; Kim, A.; Wang, Q.S.; Popovich, A.A. Synthesis of Nb-based powder alloy by mechanical alloying and plasma spheroidization processes for additive manufacturing. *Mater. Lett.* **2019**, *245*, 188–191. [[CrossRef](#)]
20. Polozov, I.; Kantyukov, A.; Goncharov, I.; Razumov, N.; Silin, A.; Popovich, V.; Zhu, J.N.; Popovich, A. Additive manufacturing of Ti–48Al–2Cr–2Nb alloy using gas atomized and mechanically alloyed plasma spheroidized powders. *Materials* **2020**, *13*, 3952. [[CrossRef](#)] [[PubMed](#)]
21. Liu, B.; Duan, H.; Li, L.; Zhou, C.S.; He, J.; Wu, H. Microstructure and mechanical properties of ultra-hard spherical refractory high-entropy alloy powders fabricated by plasma spheroidization. *Powder Technol.* **2021**, *382*, 550–555. [[CrossRef](#)]
22. Polozov, I.; Razumov, N.; Makhmutov, T.; Silin, A.; Kim, A.; Popovich, A. Synthesis of titanium orthorhombic alloy spherical powders by mechanical alloying and plasma spheroidization processes. *Mater. Lett.* **2019**, *256*, 126615. [[CrossRef](#)]
23. Makhmutov, T.; Razumov, N.; Kim, A.; Ozerskoy, N.; Mazeeva, A.; Popovich, A. Synthesis of CoCrFeNiMnW<sub>0.25</sub> High-Entropy Alloy Powders by Mechanical Alloying and Plasma Spheroidization Processes for Additive Manufacturing. *Met. Mater. Int.* **2021**, *27*, 50–54. [[CrossRef](#)]
24. Razumov, N.G.; Popovich, A.A.; Wang, Q.S. Thermal Plasma Spheroidization of High-Nitrogen Stainless Steel Powder Alloys Synthesized by Mechanical Alloying. *Met. Mater. Int.* **2018**, *24*, 363–370. [[CrossRef](#)]

25. Shelekhov, E.V.; Sviridova, T.A. Modelirovaniye dvizheniya i razogreva sharov v planetarnoy melnitse. Vliyaniye rezhimov obrabotki na produkty mekhanoaktivatsii smesi poroshkov Ni i Nb [Modeling of motion and heating of balls in planetary mill. Effect of the treatment modes on mechanoactivation products in Ni and Nb powder mixture]. *Mater. Sci.* **1999**, *10*, 13–22. (In Russian)
26. Dağdelen, F.; Malkoç, T.; Kök, M.; Ercan, E. Comparison of the transformation temperature, microstructure and magnetic properties of Co-Ni-Al and Co-Ni-Al-Cr shape memory alloys. *Eur. Phys. J. Plus* **2016**, *131*, 1–6. [[CrossRef](#)]
27. Oikawa, K.; Ota, T.; Gejima, F.; Ohmori, T.; Kainuma, R.; Ishida, K. Phase equilibria and phase transformations in new B2-type ferromagnetic shape memory alloys of Co-Ni-Ga and Co-Ni-Al systems. *Mater. Trans.* **2001**, *42*, 2472–2475. [[CrossRef](#)]
28. Popovich, A.A.; Razumov, N.G. A study of the process of mechanical alloying of iron with austenite-forming elements. *Met. Sci. Heat Treat.* **2015**, *56*, 570–576. [[CrossRef](#)]
29. Radev, D.D. Mechanical synthesis of nanostructured titanium-nickel alloys. *Adv. Powder Technol.* **2010**, *21*, 477–482. [[CrossRef](#)]
30. Kim, A.; Makhmutov, T.; Razumov, N.; Silin, A.; Popovich, A.; Zhu, J.N.; Popovich, V. Synthesis of NiTi alloy powders for powder-based additive manufacturing. *Mater. Today Proc.* **2019**, *30*, 679–682. [[CrossRef](#)]
31. Koch, C.C.; Whittenberger, J.D. Mechanical milling/alloying of intermetallics. *Intermetallics* **1996**, *4*, 339–355. [[CrossRef](#)]
32. Jiang, X.-L.; Boulos, M. Induction plasma spheroidization of tungsten and molybdenum powders. *Trans. Nonferr. Met. Soc. China* **2006**, *16*, 13–17. [[CrossRef](#)]
33. Su, J.J.; Mo, K.X.; Zhou, L. Effects of Minor Mn Replace of Al on Martensitic and Magnetic Transition in the  $\text{Co}_{38}\text{Ni}_{34}\text{Al}_{28-x}\text{Mn}_x$  Alloys. *J. Supercond. Nov. Magn.* **2020**, *33*, 835–840. [[CrossRef](#)]
34. Ju, J.; Lou, S.; Yan, C.; Yang, L.; Li, T.; Hao, S.; Wang, X.; Liu, H. Microstructure, Magnetism and Magnetic Field Induced-Strain in Er-Doped Co-Ni-Al Polycrystalline Alloy. *J. Electron. Mater.* **2017**, *46*, 2540–2547. [[CrossRef](#)]
35. Hossain, M.S.; Ghosh, T.; Kanth, B.R.; Mukhopadhyay, P.K. Effect of Annealing on the Structural and Magnetic Properties of CoNiAl FSMA. *Cryst. Res. Technol.* **2019**, *54*, 1–6. [[CrossRef](#)]
36. Saito, T. Magnetic properties of Co–Al–Ni melt-spun ribbon. *J. Appl. Phys.* **2006**, *100*, 053916. [[CrossRef](#)]
37. Arputhavalli, G.J.; Agilan, S.; Saravanan, P. Influence of sintering temperature on microstructure, magnetic properties of vacuum sintered Co (-Zn)-Ni-Al alloys. *Mater. Lett.* **2018**, *233*, 177–180. [[CrossRef](#)]